

# Cluster observations of non-time-continuous magnetosonic waves

Simon N. Walker<sup>1</sup>, Andrei G. Demekhov<sup>2,3</sup>, Scott A. Boardsen<sup>4,5</sup>, Natalia Y.

Ganushkina<sup>6,7</sup>, David G. Sibeck<sup>5</sup>, and Michael A. Balikhin<sup>1</sup>

simon.walker@sheffield.ac.uk

Simon N. Walker

<sup>1</sup>Department of Automatic Control and  
Systems Engineering, University of  
Sheffield, Sheffield. U.K.

<sup>2</sup>Polar Geophysical Institute, Apatity,  
Russia

<sup>3</sup>Institute of Applied Physics, RAS,  
Nizhny Novgorod, Russia

<sup>4</sup>Goddard Planetary and Heliophysics  
Institute, University of Maryland,  
Baltimore, Maryland, USA

<sup>5</sup>NASA/GSFC Greenbelt, Maryland, USA

This article has been accepted for publication and undergone full peer review but has not been through the copyediting, typesetting, pagination and proofreading process, which may lead to differences between this version and the Version of Record. Please cite this article as doi: 10.1002/2016JA023287

**Abstract.** Equatorial magnetosonic waves are normally observed as temporally continuous sets of emissions lasting from minutes to hours. Recent observations, however, have shown that this is not always the case. Using Cluster data, this study identifies two distinct forms of these non-temporally-continuous emissions. The first, referred to as rising tone emissions, are characterised by the systematic onset of wave activity at increasing proton gyroharmonic frequencies. Sets of harmonic emissions (emission elements) are observed to occur periodically in the region  $\pm 10^\circ$  off the geomagnetic equator. The sweep rate of these emissions maximises at the geomagnetic equator. In addition, the ellipticity and propagation direction also change systematically as Cluster crosses the geomagnetic equator. It is shown that the observed frequency sweep rate is unlikely to result from the sideband instability related to nonlinear trapping of suprathermal protons in the wave field. The second form of emissions is characterised by the simultaneous onset of activity across a range of harmonic frequencies. These waves are observed at irregular intervals. Their occurrence correlates with changes in the spacecraft potential, a measurement that is used as a proxy for electron density.

<sup>6</sup>Finnish Meteorological Institute,  
Helsinki, Finland

<sup>7</sup>University of Michigan, Ann Arbor, MI,  
USA

Thus these waves appear to be trapped within regions of localised enhancement of the electron density.

**Key points:**

- The rate of change of frequency of rising tone EMW is greatest in the vicinity of the geomagnetic equator.
- It is highly unlikely that the modulation results from the sideband instability.
- Propagation of EMW may be spatially restricted by narrow density irregularities.

Accepted Article

## 1. Introduction

Equatorial magnetosonic waves are a common occurrence over a wide range of L-shells, typically  $3 < L < 8$ , within the equatorial region of the terrestrial magnetosphere. Occurring in the frequency range between the proton gyrofrequency ( $\Omega_{cp}$ ) and the lower hybrid resonance frequency ( $\omega_{LH}$ ), they consist of a set of discrete, banded emissions at harmonics of the proton gyrofrequency [Russell *et al.*, 1969, 1970; Gurnett, 1976]. The wave normal angle ( $\theta_{Bk}$ ), the angle between the wave  $k$ -vector and external magnetic field direction, indicates the almost perpendicular propagation of magnetosonic waves. Note that in this paper, the term propagation direction refers to the wave  $k$ -vector direction rather than the group velocity direction. For cases when  $\theta_{Bk} = 90^\circ$  these two vectors will be aligned. However, for the higher harmonics (say  $N_{i10}$ ) a small deviation in  $\theta_{Bk}$  of 0.4 degrees away from 90 degrees results in the parallel group velocity component becoming the dominant component. Ray tracing shows that this causes the waves to oscillate back and forth in magnetic latitude about the magnetic equator as they propagate in the azimuthal and/or radial direction in the equatorial plane [Olsen *et al.*, 1987; Laakso *et al.*, 1990; Boardsen *et al.*, 1992; Horne *et al.*, 2000; Santolík *et al.*, 2002; Němec *et al.*, 2005; Boardsen *et al.*, 2016]. However, there are a few studies [Tsurutani *et al.*, 2014; Zhima *et al.*, 2015] suggesting the existence of low amplitude magnetosonic waves at higher latitudes. The experimentally deduced dispersion relation has been shown to agree with that based on cold plasma theory [Walker and Moiseenko, 2013; Walker *et al.*, 2015a]. Theoretical studies regarding the generation of equatorial magnetosonic waves were based on energy sources that included high energy ( $\sim 1$  MeV) ions with power law, anisotropic

distributions inside the plasmasphere [Curtis and Wu, 1979], energetic ion populations such as those observed in the ring current [Gulelmi et al., 1975], electron bounce resonant interactions Roberts and Schulz [1968], or proton ring distributions [Perraut et al., 1982; Boardsen et al., 1992; Meredith et al., 2008; Horne et al., 2000; Chen et al., 2010, e.g.] with  $\partial f/\partial v_{\perp} > 0$  for energies of a few 10's of keV. Recent Cluster observations reported by Balikhin et al. [2015] have demonstrated that the observed wave spectrum matches that predicted based on the observed proton ring distribution. Equatorial magnetosonic waves have also been shown to be generated via proton shell distributions [Min and Liu, 2016] resulting in a more complex frequency/wavenumber growth pattern.

It is currently assumed that equatorial magnetosonic waves interact with the local electron population, efficiently accelerating some particles to high energies while scattering others into the loss cone [Horne et al., 2007; Mourenas et al., 2013]. These interactions may be successfully modelled using quasilinear theory since there is sufficient overlap between the emissions at adjacent harmonics of the proton gyrofrequency [Walker et al., 2015b].

Almost all previous descriptions of the occurrence of magnetosonic waves have shown that these emissions occur continuously over periods from a few minutes to hours. There have been only two exceptions to this. The first was the observation of magnetosonic wave trapping inside the plasmopause [Ma et al., 2014]. Ma et al. [2014] demonstrated that magnetosonic waves generated locally inside the plasmopause boundary may propagate inward, eventually becoming trapped within a limited radial region of the outer plasmasphere by large scale density structures. Further evidence was also presented for the trapping by small scale structures. The second type of non-temporally continuous

observations of magnetosonic waves are the recently identified observations of rising tone magnetosonic waves by *Fu et al.* [2014], *Boardsen et al.* [2014], and *Němec et al.* [2015] based on observations from THEMIS, Van Allen Probes, and Cluster respectively. These emissions are observed as a set of rising tone elements, much the same as rising chorus elements [*Li et al.*, 2011] or EMIC waves [*Nakamura et al.*, 2014]. However, the observations presented by these authors can not resolve the true, discrete banded nature of the spectrum of magnetosonic waves. These observations show the occurrence of individual elements whose frequency rises with time with a sweep rate of 1 Hz/s in a similar manner as has been observed for chorus emissions. These sets appeared to be modulated with a repetition time of the order 2-3 minutes with the emission elements turning on and off.

The present paper investigates the occurrence of non-temporally continuous observations of magnetosonic waves. Section 2 outlines the sources of data used in this study. Sections 3 and 4 present Cluster observations of rising tone emissions and trapped emissions respectively. Section 5 compares these observations with those from THEMIS and the Van Allen probes results, showing that the nature of the waves changes with distance from the magnetic equator. Potential modulation mechanisms for the rising tone emissions are briefly mentioned. It is shown that one particular mechanism, namely the side band instability that results from the nonlinear trapping of particles and has been used to explain the frequency drift in chorus emissions, may probably be ruled out as a possible mechanism. The results and discussion are then summarized in Section 6.

## **2. Data source**

The data presented here were collected by the fluxgate magnetometer (FGM) [*Balogh et al.*, 1997], the STAFF (Spatio-Temporal Analysis of Field Fluctuations) search coil mag-

netometer [Cornilleau-Wehrlin *et al.*, 1997], and the Electric Fields and Waves (EFW) [Gustafsson *et al.*, 1997] instruments, on board the multi-spacecraft Cluster mission [Escoubet *et al.*, 1997]. Synchronisation of the STAFF and EFW sampling is achieved via the centralised Wave Experiment Consortium Digital Wave Processor instrument [Wooliscroft *et al.*, 1997]. Launched in the year 2000, the four Cluster spacecraft follow a polar orbit, with an apogee of  $\sim 20R_E$ , initial perigee  $\sim 4R_E$  and period of 57 hours. This initial orbit has evolved over time as the line of apsides has rotated southward before rising again in 2010 and its perigee falling to a minimum of 200 km in the same time period. These changes have allowed Cluster to sample plasma and wave activity at the magnetic equator over a range of different radial distances. The observations presented here were made during periods when the satellites were operated in burst science mode (BM1). This operational mode allows FGM and STAFF to collect magnetic field waveform measurements with sampling rates of 67 Hz and 450 Hz respectively. In this paper the spacecraft potential from the EFW instrument is used as a proxy for the electron density [Pedersen *et al.*, 2001].

### 3. Observations of rising tone emissions

The first event discussed in this paper occurred on 18 August 2005 and was observed by Cluster 1 between 13:50 and 14:00 UT and Cluster 2 between 13:00 to 13:30 UT (BM1 operations were scheduled for the period 13:00-14:00 UT on all four spacecraft). Table 1 gives the locations of Cluster 1 and 2. The Cluster satellites were travelling in a south to north direction, crossing the magnetic equator at 14:06:00 UT (C1) and 13:14:16 UT (C2). Examination of the electric field spectrogram recorded by the WHISPER instrument (not shown) shows that the electron plasma frequency maximises around 13:40 UT at a value

of  $\sim 42$  kHz, which would imply an electron density of the order  $21 \text{ cm}^{-3}$  indicating that C2 came close to the plasmopause but never actually crossed into the plasmasphere itself. These observations occurred during a period of low to medium geomagnetic activity for which the maximum (negative) value of Dst in the preceding 24 hrs was  $-16 \text{ nT}$  whilst the AE index over the preceding 36 hours maximised at  $531 \text{ nT}$  (mean  $284 \text{ nT}$ ). Using these values within the *O'Brien and Moldwin* [2003] plasmopause model shows that C2 was very close to the expected location of the equatorial plasmopause.

Figure 1 shows an overview of measurements from the Cluster 2 spacecraft. Figure 1a shows a spectrogram of the magnetic field oscillations recorded in the  $B_Z$  component (Geocentric Solar Ecliptic, GSE) by the STAFF search coil magnetometer. The white horizontal lines show harmonics of the local proton gyrofrequency in the range 7 to 30, with labels towards the left side of the spectrogram. The solid vertical black line indicates the time at which the magnetic equator was crossed, the dotted vertical black lines indicate the times of the spectra shown in Figure 2. Figure 1b shows the ellipticity (ratio of the intermediate ( $e_{int}$ ) and maximum ( $e_{max}$ ) eigenvalues of the spectral matrix) of the oscillations. For the periods when the banded emissions are observed, the ellipticity is low  $e_{int}/e_{max} < 0.2$ , indicating highly elliptical polarization. Figure 1c shows the angle between the wave vector direction and the external magnetic field. These emissions show a strong preference for propagating in a direction almost perpendicular to the external magnetic field. Finally, Figure 1d shows the angle between the maximum variance direction (which corresponds to the plane in which the wave magnetic field oscillates) to the external magnetic field. For the oscillations discussed in this paper, the wave magnetic



field is aligned with the external magnetic field. These properties are all consistent with previous observations [*Boardsen et al.*, 2016, e.g.].

In Figure 1a two types of equatorial magnetosonic waves with different frequency and temporal characteristics can be distinguished. At frequencies above 40 Hz, the emissions are observed to occur as a number of rising tone elements. A series of  $\sim 11$  rising tone emission elements are observed between 13:05 and 13:13 UT. Each individual element consists of a set of emissions at harmonics of the local proton gyrofrequency that are observed first at lower frequencies ( $\sim 15\Omega_P$ ), gradually rising to  $\sim 30\Omega_P$  in the space of 35-40 s for most elements with some taking as long as 90 s. These elements also show evidence for a temporal structure with a periodic cycle of around 110-130 seconds, a value similar to that reported by *Boardsen et al.* [2014] and *Fu et al.* [2014].

It is noticeable that the characteristic properties of the harmonic emissions changes from one element to the next. The wave power of these emissions in individual elements is largest for the three elements observed around 13:15 UT, the time at which Cluster 2 crossed the geomagnetic equator. On either side the power reduces significantly with the distance of Cluster 2 from the equator. These three 'central' elements also appear to possess a greater ellipticity and their propagation direction appears to be closer to perpendicular than the elements that are observed a few degrees north or south of the equator.

At frequencies less than 40 Hz there is a set of continuous, banded emissions in the period 13:05-13:27 UT. Their amplitude is typically greater than 3 pT, varying throughout the period but less than that typically reported [*Mourenas et al.*, 2013; *Zhima et al.*, 2015, e.g.]. Between 13:10 and 13:12 UT the strongest emissions appear to be centred at the

proton gyroharmonic frequencies in the range 7-10 inclusive. It is also noticeable that there are other bands that appear roughly in the centre between two consecutive proton gyrofrequencies. After 13:15 UT, and particularly around 13:20 UT, the frequency of the bands begins to decrease in contrast to the proton gyrofrequency harmonics (white lines).

Figure 2 shows average power spectra of emissions observed in the time periods 13:13:30.8-13:14:28.9 UT (Figure 2a), 13:16:25.0-13:18:00.4 UT (Figure 2b), and 13:26:34.7-13:28:39.1 UT (Figure 2c), as indicated by the vertical dotted lines in Figure 1, computed using a 1024 point Fast Fourier Transform (FFT) during which three individual periodic elements were observed. The red vertical lines mark the even harmonics of the proton gyrofrequency in the range 2-30. The discrete harmonic nature of the waves is clearly seen with emissions occurring at or very close to harmonics of the proton gyrofrequency. Most of the spectral peaks are narrow, typically 2.5 Hz wide. However, some peaks, especially those below 40 Hz are considerable wider. For the emissions observed in the period 13:13:30.8-13:14:28.9 UT (panel a in Figure 2) there are peaks observed at frequencies of (approx) 25.4, 26.8, 28.5, 30.5, 32.5, 36.5, 38.5, 40.6, 44.3 Hz with the frequency spacings between peaks of either  $\sim 4$  or 2 Hz. These frequencies correspond to the local proton and alpha particle gyrofrequencies, respectively. Thus, these emissions may be observed at their point of generation. Similar frequency spacings are also evident in the spectra shown in Figure 2b and c.

A second set of similar emissions was observed on 16 September 2005 between 03:40 and 04:00 UT by C1. The locations of the Cluster 1 and 2 satellites during this period are given in Table 1 and they crossed the magnetic equator at around 03:51:32 and 02:56:33 UT respectively. Figure 3 shows the occurrence of the emissions and their properties using the

same format as Figure 1. Figure 3a clearly shows two sets of emissions, one continuous and the other periodic. Figure 3b-d show the ellipticity ( $e_{int}/e_{max} < 0.2$ ), a wave vector direction almost perpendicular to that of the external magnetic field, and the direction of the maximum variance of the wave oscillations aligned with the magnetic field, all features consistent with observations of equatorial magnetosonic waves.

In this particular case, a set of continuous emissions occurs at higher frequencies (between  $28\Omega_P < \omega < 31\Omega_P$ ) than the periodic discrete rising tone emissions ( $21\Omega_P < \omega < 27\Omega_P$ ). This is similar to the observations presented by *Boardsen et al.* [2014] and *Fu et al.* [2014]. The continuous tone emissions appear to be centred on the local proton harmonic frequencies, except at times when the sets of rising tones intersect these frequencies in which case the emission is observed slightly above the gyroharmonic. Thus, it appears that, once again, the satellite is passing through the source region of these emissions. Below these continuous emissions, there are a number of sets of periodic emissions, occurring with a period of around 80-90 seconds. The discrete frequency of emission increases with time at a rate of  $\approx 0.5-0.8$  Hz/s. The amplitude of these emissions varies by 2-3 orders of magnitude, the strongest being observed as the satellite crosses the magnetic equator.

On 16 September 2005, C2 crossed the magnetic equator around 02:56:33 UT, almost an hour before C1. A similar set of emissions was observed (not shown). Continuous emissions were observed in the frequency range (between  $26\Omega_P < \omega < 32\Omega_P$ ), mirroring changes observed in the local proton gyrofrequency. Below this frequency range there are two or three bands at the 22, 23, and 24 harmonics in which emissions occur periodically with the higher amplitudes occurring around the time at which the satellite crossed the

magnetic equator. These periodic waves show fleeting evidence for the rising tone structure seen so prominently by C1.

#### 4. Observations of trapped emissions

Cluster 1 observed a second type of non-time-continuous equatorial magnetosonic emissions on 13 September 2005, as shown in Figure 4. Table 1 gives the location of Cluster 1 at this time. The horizontal white lines indicate harmonics of the proton gyrofrequency in the range 15 to 35, numbered towards the left of the panel and the black vertical line indicates the time at which the geomagnetic equator was crossed. The red line shows the spacecraft potential (with a scale on the right hand Y axis) measured by the EFW instrument. This data set is used as a proxy for the electron density. The more positive the spacecraft potential, the higher the electron density [Pedersen *et al.*, 2001]. The wave spectrogram shows there are sets of strong emissions observed at 17:56:24, 17:58:57, 18:00:29, 18:01:53, 18:03:37, 18:05:32, and 18:07:30 UT. These sets do not occur periodically, the time difference between them varying between 1.5 to 3 minutes. It is noticeable that the onset times of the emissions at different harmonic frequencies are simultaneous, in contrast to the rising tone emissions shown in Figures 1 and 3. Analysis of the properties for these waves (not shown) reveals that they are highly elliptical, propagate almost perpendicularly to the background magnetic field and that their magnetic component is directed parallel to the background magnetic field. These properties clearly demonstrate that the observed emissions are equatorial magnetosonic waves.

At lower frequencies, below 80 Hz, the emissions occur at harmonics of the local proton gyrofrequency and are also seen to track the changes of these frequencies. For example, in the set of emissions observed at around 18:05:30 UT emissions are observed at the 19-27

harmonics and the frequency of the emission is observed to increase in response to that observed in the local proton gyrofrequency. The first set, observed at 17:56:24 UT, shows three clear bands at frequencies of 92.9, 96.1, and 99.2 Hz. The frequency spacing of these emissions ( $\sim 3.1$  Hz) is slightly different to the local proton gyrofrequency ( $\sim 3$  Hz) and they are observed between the local gyroharmonics. Therefore it appears as if these emissions originate elsewhere and have propagated to the point of observation. The sets of emissions observed at 17:58:57 UT, and 18:00:29 UT are all characterised by waves occurring at the gyroharmonics in the ranges 26-32 and 21-29, respectively. At frequencies above 80 kHz, the structure of emissions is much more complex. The emissions appear not to be tied closely to the local harmonics of the proton gyrofrequency anymore. These banded emissions exhibit both rising and falling tones. However, a more detailed analysis of these emissions is left for future work.

Figure 5 shows a second period during which sporadic occurrences of magnetosonic waves were observed by Cluster 3 on 17 September 2006. The format of the figure is the same as Figure 4. At this time Cluster 3 was located inside the plasmopause (having crossed the boundary at around 13:30 UT). Cluster 3 crossed the magnetic equator at around 14:42:30 UT on the dayside, at a location (4.2, -0.2, 0.0)Re (Solar Magnetic coordinates, SM).

The background spectrogram in Figure 5 shows the emissions recorded by the STAFF search coil magnetometer. The strongest emissions are observed at lower frequencies ( $< 40$  Hz) between around 14:30 and 14:50 UT. The frequency structure of these emissions shows bands that occur roughly at harmonics of the proton gyrofrequency. It is also noticeable that there are other bands occurring between these harmonics, possibly

indicating resonance with heavier ions such as  $\text{He}^+$ , or  $\text{He}^{2+}$ . Just before 14:30 UT there is a set of emissions whose peak amplitudes lie at frequencies up to the 20 harmonic of the proton gyrofrequency.

In addition to these long lived emissions, there are several examples of banded emissions that are observed for less than a minute. Table 2 lists the periods when these emissions were observed, together with their mean frequency spacing ( $\delta f$ ) and the local gyrofrequency ( $\Omega_P$ ). From these results it can be seen that the frequency spacing of the bands is either less than or greater than the local gyrofrequency and so it appears as if these emissions have propagated from their source region to the point of observation. It is also noticeable that at the beginning of the period the frequency spacing is less than the local gyrofrequency which would imply generation at a greater radial distance whilst at the end of the period the frequency spacing is greater than the gyrofrequency, indicating generation at smaller radial distances.

Superimposed on top of the spectrogram in Figure 5 is the spacecraft potential as measured by EFW. A comparison of the occurrence of the sporadic magnetosonic emissions discussed above with changes observed in the satellite potential shows that, in general, most of the sets of wave emissions are coincident with local increases in the spacecraft potential and, hence, with increases in the local electron density. This is probably best illustrated by the sets of emissions occurring at 14:20:19–14:21:18 UT. In this particular period, there are two local peaks in the spacecraft potential. While the wave emissions occur throughout this period, it can be seen that the maximum amplitudes are coincident with the peaks in spacecraft potential. At other times it appears that the waves tend to occur at times of steep gradients in the spacecraft potential. For this particular set of

observations this seems to be the most common correlation. For instance, the emissions observed between 14:12:09 and 14:12:47 UT begin when the value of the spacecraft potential is at a maximum and continue until the following minima in the potential. Between 14:22:03 and 14:22:44 UT there is another large peak in the potential. Again, the intensity of the wave emissions is largest during the periods in which the change in potential is greatest. Thus, it appears that the magnetosonic waves are spatially confined within localised regions of increased spacecraft potential and hence electron density.

## 5. Discussion

In the previous sections observations of non-time continuous magnetosonic waves by the Cluster satellites were presented. The observations show two different types of non-time continuous magnetosonic waves.

### 5.1. Rising tone emissions

In Section 3 examples of rising tone emissions were presented. Similar emissions have been reported by *Boardsen et al.* [2014], *Fu et al.* [2014] and *Němec et al.* [2015] based on Van Allen Probes, THEMIS, and Cluster measurements, respectively. However, whilst these previous reports first showed the existence of these periodic structures, they were unable to show the frequency structure of the emissions. The observations reported by *Boardsen et al.* [2014] and *Fu et al.* [2014] show a large number of elements whereas only a small number of emission elements are seen by Cluster. This difference can be understood in terms of the mission orbits. Due to its polar orbit, Cluster typically observed around 10 elements of emissions in contrast to the long trains observed by the equatorial spacecraft Van Allen and THEMIS. During the first 12 years of operations, the four Cluster spacecraft

were only able to make 5 observations of such waves while operating in science Burst Mode 1. However, all five observations were situated on the dayside, within 1.5 hours of local noon (SM) and in the vicinity of the model [O'Brien and Moldwin, 2003] plasmapause. The Cluster observations were restricted to within  $10^\circ$  of the magnetic equator, a result inline with the theory of propagation of magnetosonic waves. In all cases the most intense emissions were observed close to the equatorial crossing.

The rising tone emissions observed by Cluster occurred in conjunction with observations of time continuous magnetosonic waves, although, this is not always the case [Němec et al., 2015]. These continuous emissions were observed at either higher or lower frequencies than the rising tone emissions. The frequency of the discrete components that make up each element of the rising tone emissions appears to mirror the changes observed in the local proton gyrofrequency harmonics, indicating local generation. However, in the case of the continuous emissions the relationship between the emissions and the harmonics of the local proton gyrofrequency was less clear. Sometimes their frequency followed changes in the local gyrofrequency, indicating local generation whilst at other times it appeared to change independently, indicative of remote generation and propagation to the point of observation.

To investigate the sweep rate, i.e. how the occurrence of the individual tones within an element varies with time, the time and frequency for the maximum amplitude of each tone occurred was determined. The upper panel of Figure 6 shows how the observation time varies as a function of frequency for six of the rising tone elements observed by Cluster 2 on 18 August 2005 in the vicinity of the geomagnetic equator. The lower panel shows the magnetic latitude of Cluster 2 with the redline representing the equator. The



black vertical line on both panels marks the time at which Cluster 2 crossed the magnetic equator. For each element, a least squares fit was performed to determine the frequency sweep rate. For these emission elements the frequency sweep rate varies in the range  $\delta f/\delta t \approx 0.3 - 0.9 \text{ Hz s}^{-1}$ . The legend in Figure 6 indicates the sweep rate determined for each element. It is noticeable that when the satellite is closest to the equator, the sweep rate is higher. For instance, from Figure 6 it is seen that for the element observed closest to the equator (element 3) the sweep rate is  $\approx 1 \text{ Hz s}^{-1}$ , a value similar to that reported by *Fu et al.* [2014]. However, as the observation point moves further away from the equator the sweep rate becomes smaller.

Due to their differing orbits, the four Cluster spacecraft cross the magnetic equator at different times. As mentioned above, for the first example of rising tone emissions observed on 18 August 2005, C2 crossed at  $\sim 13:14:16$  UT while Clusters 1, 3, and 4 crossed at  $14:06:00$ ,  $16:04:57$ , and  $16:16:09$  UT, respectively. Since these crossings occurred outside the window for burst mode operations, high resolution waveforms are unavailable at these times. However, C1 did begin to observe rising tone magnetosonic waves from around  $13:49$  UT until the end of burst mode operations at  $14:00$  UT, about 45 minutes after they were observed by C2. The location at which each spacecraft crossed the equator differed by  $\sim 3000$  km, almost entirely in the Y-SM direction with C1 slightly further duskward than C2 and at a slightly greater radial distance (see Table 1). In the case of the second rising tone event presented above, the Cluster 1 and 2 satellites crossed the equator at locations spatially separated by around  $2400$  km, mainly in the SM-Y direction ( $2300$  km) and almost an hour temporally. However, it is not certain whether the emissions observed by the pairs of Cluster satellites in each period correspond to the

same or different source regions and no firm conclusions regarding the size, lifetime, or motion of the source region can be made.

The generation mechanism for these rising tone emissions is unclear. The proposed mechanisms include

1. The appearance of these waves may be due to either their propagation from their source region to the point of observation, especially if the propagation path includes multiple reflections within the plasmopause wave guide. However, this would only explain the upper range of observed harmonics [*Boardsen et al.*, 2014].

2. The modulation and frequency characteristics could result from a saw-tooth ULF wave, which would modify the local Alfvén velocity accordingly, turning the instability gradually on and off [*Boardsen et al.*, 2014].

3. By processes such as quasilinear particle diffusion, analogous to that proposed for pulsating aurorae [*Demekhov and Trakhtengerts*, 1994].

4. By mechanisms similar to those proposed for the generation of rising tones in chorus emissions e.g. electron cyclotron maser [*Trakhtengerts*, 1995] or the sideband instability [*Trakhtengerts*, 1999] that result from the trapping of particles by a quasi-monochromatic wave.

In the following discussion, the sideband instability is considered in depth and it is shown that this mechanism may probably be ruled out as a possible source for the generation of rising tone equatorial magnetosonic waves.

If a wave packet is quasi-monochromatic, then it can trap charged particles [*Karpman and Shklyar*, 1972, e.g.] (and references therein) in a finite range of velocities near the resonance. The trapped particle distribution function is flattened in this range, and either

a plateau or a valley forms in this region, depending on the initial distribution and other factors such as the inhomogeneity of the medium. The distribution function attains larger velocity space gradients on the boundaries of the trapping region, which gives rise to upper and lower sidebands shifted in frequency with respect to the original wave. The frequency shift is of the order of the nonlinear oscillation frequency  $\Omega_{\text{tr}}$  of charged particles trapped in the wave field (trapping frequency) [Karpman *et al.*, 1974, e.g.].

This phenomenon known as the sideband instability can become recursive if the initial wave is strong enough. In this case, each sideband can give rise to other sidebands, and a rising or falling tone can be formed from the sequence of sidebands. Such a mechanism was proposed to explain the frequency drift in VLF chorus emissions [Trakhtengerts, 1999; Trakhtengerts *et al.*, 2004], and hydromagnetic chorus [Trakhtengerts *et al.*, 2007].

Since the distribution function of trapped particles flattens in about one trapping period,  $\delta t \sim 2\pi/\Omega_{\text{tr}}$ , and every sideband is shifted by  $\delta\omega \sim \Omega_{\text{tr}}$  from the previous one, the corresponding estimate for the frequency drift is

$$\partial\omega/\partial t \simeq \Omega_{\text{tr}}^2/(2\pi) \quad (1)$$

where  $\Omega_{\text{tr}}$  is the frequency of charged particle oscillations in the wave field (trapping frequency) [Karpman *et al.*, 1974]. For example, for parallel propagating waves

$$\Omega_{\text{tr}}^2 = ekv_{\perp}B_w/(mc), \quad (2)$$

where  $B_w$  is the wave magnetic field amplitude,  $k$  is the wave number,  $v_{\perp}$  is the particle velocity transverse to the external magnetic field,  $e > 0$  and  $m$  are the elementary charge and particle mass, and  $c$  is the speed of light in free space.

A similar result for the chorus frequency drift rate have been obtained by *Omura et al.* [2008] who calculated the nonlinear growth rate of a whistler-mode wave with frequency drift under the assumption of a flat distribution function of trapped electrons, and found the frequency drift rate corresponding to the maximum growth rate. Note that, while Eq.(1) was obtained as an order of magnitude estimate, more rigorous calculations by *Omura et al.* [2008] yielded a correction coefficient to it which is close to unity.

Equation (1) has been used to estimate the possible role of nonlinear trapping effects in the observed frequency drift of magnetosonic waves.

The appropriate methodology for calculating the trapping frequency can be found, for example, in the review paper by *Shklyar and Matsumoto* [2009]. In what follows we adopt a similar formulation to that used in *Artemyev et al.* [2015].

After expansion over small wave amplitude the normalized Hamiltonian takes the form

$$\mathcal{H} = \mathcal{H}_0 - b_w \sum_n W_n \cos(\phi + n\varphi), \quad (3)$$

where

$$\mathcal{H}_0 = \gamma = \sqrt{1 + u_{\parallel}^2 + u_{\perp}^2} \quad (4)$$

is the unperturbed Hamiltonian,  $u_{\parallel,\perp} = p_{\parallel,\perp}/(mc)$  are the normalized momentum components parallel and perpendicular to the magnetic field,

$$b_w = \frac{eB_w}{mc^2k} \quad (5)$$

is the normalized value of the wave magnetic field  $B_w$ , and  $\varphi$  is the particle gyrophase.

The perpendicular momentum is related to the first adiabatic invariant as  $u_{\perp}^2 = 2\chi I_{\perp} b$ , where  $\chi = \Omega_{eq} R_0/c$ ,  $b = B(z)/B_{eq}$  is the dimensionless external magnetic field,  $I_{perp}$  is the first adiabatic invariant,  $\zeta = z/R_0$  is the normalized spatial coordinate along the magnetic

field,  $\Omega_{eq} = eB_{eq}/(mc)$  is the equatorial gyrofrequency, and  $R_0$  is the spatial scale chosen for normalization (e.g.,  $R_0 = R_E L$  where  $R_E$  is the Earth radius). The wave phase is  $\phi = \chi(kz \cos \theta - \omega t)$ , where  $\theta$  is the wave normal angle.

The summation in the wave-particle interaction term in Eq. (3) is performed over the gyroresonance harmonics, and the interaction coefficient for the  $n$ -th resonance can be expressed in the form

$$W_n = \frac{u_{\perp}}{\gamma} J'_n(\xi) + aN^{-1} \left( 1 - \frac{n\Omega_{eq}}{\gamma\omega \sin \theta} \right) J_n(\xi) \quad (6)$$

Here  $a \simeq -N^2\omega\omega_{Be}/\Omega_e^2$  is the coefficient determined by the wave polarization (the subscript  $e$  denotes the electron values), for which we use an approximate formula valid for the magnetosonic waves with frequencies  $\omega \lesssim \omega_{LH}$  ( $\omega_{LH}$  is the lower-hybrid resonance frequency),  $N = kc/\omega$  is the wave refractive index,  $J_n$  is a Bessel function of the first kind of the order  $n$ , and  $\xi = N \sin \theta u_{\perp}\omega/\Omega_{eq}$ .

Using this Hamiltonian, it is easy to obtain the trapping frequency for an isolated  $n$ -th gyroresonance in the form

$$\Omega_{tr n}^2 = N\omega \cos^2 \theta \frac{eB_w}{mc} |W_n|. \quad (7)$$

Equation (7) is used to calculate the trapping frequency for the observed MS waves. From Section 3, we have the plasma density  $N_c \simeq 1.9 \cdot 10^3 \text{ cm}^{-3}$ , the geomagnetic field  $B = 205 \text{ nT}$ , and the wave magnetic field  $B_w = 1.5 \text{ nT}$ . The wave refractive index  $N$  can be calculated as

$$N^2 \simeq \frac{N_A^2}{1 - \omega^2/\omega_{LH}^2}, \quad (8)$$

where  $N_A^2 = \omega_{p\alpha}^2/\omega_{B\alpha}^2$  is the Alfvén refractive index, and  $\alpha$  is the particle species index over which, generally speaking, summation is performed (however, mainly protons of ambient plasma determine  $N_A^2$  in the magnetosphere).

If we assume a wave normal angle of  $\theta = 89^\circ$ , then over a broad range of wave frequencies, gyroharmonic numbers, and proton energies, we obtain  $\Omega_{\text{tr}} \lesssim 0.1$  to  $1 \text{ s}^{-1}$ . This is illustrated in Figure 7 for different perpendicular energies of suprathermal protons. The parallel energies are determined by the cyclotron resonance condition, and the harmonic number was chosen according to the gyroresonance closest to the given frequency. These resonant energies are plotted in Figure 8. The frequency dependence of  $\Omega_{\text{tr}}$  is determined by two oscillatory factors, one being related to the change of a harmonic number, and the other one to the Bessel function. As a result, the estimate for the frequency drift related to nonlinear trapping is

$$\frac{1}{2\pi} \frac{\partial \omega}{\partial t} \lesssim 0.025 \text{ Hz s}^{-1}. \quad (9)$$

Since this sweep rate is an order of magnitude smaller than that observed it seems fairly unlikely that the rising tone equatorial magnetosonic waves results from the sideband instability.

## 5.2. Trapped emissions

Examples of the second type of non-time-continuous magnetosonic emissions were shown in Section 4. These emissions were characterised by being observed at all harmonic frequencies simultaneously and being more sporadic in their occurrence, in contrast to the rising tone emissions. These emissions occurred simultaneously with increases in the satellite potential, implying the existence of localised enhancements in the electron density.

One possible explanation for this non-periodic, time-discontinuous behaviour of the waves is related to the fact that the waves may become trapped within localised density structures. It was shown by *Chen and Thorne* [2012] that it is possible for magnetosonic waves to be trapped by the density changes encountered at the inner edge of the plasma-

pause boundary layer, thus limiting the radial extent of their propagation. This was investigated further by *Ma et al.* [2014] who showed that magnetosonic waves generated in the vicinity of the plasmopause, becoming trapped within a small radial distance of the outer plasmasphere. These authors also showed the magnetosonic waves may be trapped in localised regions of enhanced density.

Both sets of observations presented above show evidence for the short lived multi-harmonic magnetosonic wave emissions are observed simultaneously with local peaks in the measurements of the satellite potential. Hence, it appears that the emissions are confined by the width of these 'density' peaks.

## 6. Conclusions

Examples of non-time continuous emissions of equatorial magnetosonic waves have been presented. It was shown that two forms of such waves can be distinguished, namely, rising tone and trapped emissions.

Rising tone emissions are characterised by the fact that higher harmonic frequencies appear slightly later than those at lower frequencies, resulting in a stepped appearance due to their discrete nature. Cluster observations show that they occur at low magnetic latitudes, typically within  $10^\circ$  of the magnetic equator. Their properties were observed to change as the satellites approached and then receded the geomagnetic equator. The emissions at the equator were shown to have higher amplitudes, higher ellipticity, and propagate closer to perpendicular than similar emissions observed at higher latitudes.

It was shown that the sweep rate of these emissions is greatest in the vicinity of the geomagnetic equator. The sideband instability was considered as a possible generating mechanism for these rising tone emissions. However, calculations show that the theoretical

sweep rate is much lower than that observed, thus implying that this mechanism is unlikely to be the cause of these emissions. Emission elements occur periodically, however the cause of this periodicity is uncertain.

Trapped magnetosonic emissions are characterised by the simultaneous onset of wave activity over a range of harmonic frequencies, in contrast to the rising tone structures.

The sporadic nature of these emissions correlates with changes in measurements of the spacecraft potential, a parameter that is used as a proxy for the electron density. Periods during which the sporadic emissions were observed to be coincident with increases in the spacecraft potential (and hence electron density). Hence the wave emissions appear to be confined to regions of higher electron density.

**Acknowledgments.** The research performed by SNW, MAB, and NYG has received funding from the European Union Horizon 2020 Research and Innovation programme under grant agreement 637302 PROGRESS. MAB, NYG and AGD wish to thank the International Space Science Institute in Bern, Switzerland, for their support of the international team on "Analysis of Cluster Inner Magnetosphere Campaign data, in the application the dynamics of waves and wave-particle interaction within the outer radiation belt". MAB also acknowledges funding for DWP Cluster operations from ESA and STFC ST/N002865/1. The work of AGD was supported by the Russian Science foundation. The contribution from SAB undertaken at GSFC was supported by NASA prime contract NAS5-01072. DGS acknowledges that portions of the work at NASA/GSFC were funded by the Van Allen Probes mission. The data analysed in this paper are publicly available from the Cluster Science Archive (<http://www.cosmos.esa.int/web/csa>).



## References

- Artemyev, A. V., D. Mourenas, O. V. Agapitov, and V. V. Krasnoselskikh (2015), Relativistic electron scattering by magnetosonic waves: Effects of discrete wave emission and high wave amplitudes, *Physics of Plasmas*, *22*(6), 062901, doi:10.1063/1.4922061.
- Balikhin, M. A., Y. Y. Shprits, S. N. Walker, L. Chen, N. Cornilleau-Wehrin, I. Dandouras, O. Santolik, C. Carr, K. H. Yearby, and B. Weiss (2015), Observations of discrete harmonics emerging from equatorial noise, *Nat Commun*, *6*, doi:10.1038/ncomms8703.
- Balogh, A., M. W. Dunlop, S. W. H. Cowley, D. J. Southwood, J. G. Thomlinson, K. H. Glassmeier, G. Musmann, H. Lühr, S. Buchert, M. H. Acuña, D. H. Fairfield, J. A. Slavin, W. Riedler, K. Schwingenschuh, and M. G. Kivelson (1997), The Cluster magnetic field investigation, *Sp. Sci. Rev.*, *79*, 65–91, doi:10.1023/A:1004970907748.
- Boardsen, S. A., D. L. Gallagher, D. A. Gurnett, W. K. Peterson, and J. L. Green (1992), Funnel-shaped, low-frequency equatorial waves, *J. Geophys. Res.*, *97*, 14,967, doi:10.1029/92JA00827.
- Boardsen, S. A., G. B. Hospodarsky, C. A. Kletzing, R. F. Pfaff, W. S. Kurth, J. R. Wygant, and E. A. MacDonald (2014), Van allen probe observations of periodic rising frequencies of the fast magnetosonic mode, *Geophys. Res. Lett.*, *41*, 8161–8168, doi:10.1002/2014GL062020.
- Boardsen, S. A., G. B. Hospodarsky, C. A. Kletzing, M. J. Engebretson, R. F. Pfaff, J. R. Wygant, W. S. Kurth, T. F. Averkamp, S. R. Bounds, J. L. Green, and S. De Pascuale (2016), Survey of the frequency dependent latitudinal distribution of the fast magnetosonic wave mode from van allen probes electric and magnetic field instrument

and integrated science waveform receiver plasma wave analysis, *J. Geophys. Res. (Space Physics)*, *121*, 2902–2921, doi:10.1002/2015JA021844.

Chen, L., and R. M. Thorne (2012), Perpendicular propagation of magnetosonic waves, *Geophys. Res. Lett.*, *39*, L14102, doi:10.1029/2012GL052485.

Chen, L., R. M. Thorne, V. K. Jordanova, and R. B. Horne (2010), Global simulation of magnetosonic wave instability in the storm time magnetosphere, *J. Geophys. Res. (Space Physics)*, *115*(A11), A11222, doi:10.1029/2010JA015707.

Cornilleau-Wehrin, N., P. Chauveau, S. Louis, A. Meyer, J. M. Nappa, S. Perraut, L. Rezeau, P. Robert, A. Roux, C. De Villedary, Y. de Conchy, L. Friel, C. C. Harvey, D. Hubert, C. Lacombe, R. Manning, F. Wouters, F. Lefeuvre, M. Parrot, J. L. Pinçon, B. Poirier, W. Kofman, P. Louarn, and the STAFF Investigator Team (1997), The Cluster Spatio-Temporal Analysis of Field Fluctuations (STAFF) experiment, *Sp. Sci. Rev.*, *79*, 107–136.

Curtis, S. A., and C. S. Wu (1979), Gyroharmonic emissions induced by energetic ions in the equatorial plasmasphere, *J. Geophys. Res.*, *84*, 2597–2607, doi:10.1029/JA084iA06p02597.

Demekhov, A. G., and V. Y. Trakhtengerts (1994), A mechanism of formation of pulsating aurorae, *J. Geophys. Res.*, *99*, 5831–5841, doi:10.1029/93JA01804.

Escoubet, C. P., R. Schmidt, and M. L. Goldstein (1997), Cluster - Science and mission overview, *Sp. Sci. Rev.*, *79*, 11–32.

Fu, H. S., J. B. Cao, Z. Zhima, Y. V. Khotyaintsev, V. Angelopoulos, O. Santolik, Y. Omura, U. Taubenschuss, L. Chen, and S. Y. Huang (2014), First observation of rising-tone magnetosonic waves, *Geophys. Res. Lett.*, *41*(21), 7419–7426, doi:

10.1002/2014GL061687.

Gulelmi, A. V., B. I. Klaine, and A. S. Potapov (1975), Excitation of magnetosonic waves with discrete spectrum in the equatorial vicinity of the plasmopause, *Planet. Sp. Sci.*, *23*, 279–286, doi:10.1016/0032-0633(75)90133-6.

Gurnett, D. A. (1976), Plasma wave interactions with energetic ions near the magnetic equator, *J. Geophys. Res.*, *81*, 2765–2770, doi:10.1029/JA081i016p02765.

Gustafsson, G., R. Boström, B. Holback, G. Holmgren, A. Lundgren, K. Stasiewicz, L. Åéhlen, F. S. Mozer, D. Pankow, P. Harvey, P. Berg, R. Ulrich, A. Pedersen, R. Schmidt, A. Butler, A. W. C. Fransen, D. Klinge, M. Thomsen, C.-G. Falthamar, P.-A. Lindqvist, S. Christenson, J. Holtet, B. Lybekk, T. A. Sten, P. Tanskanen, K. Lappalainen, and J. Wygant (1997), The Electric Field and Wave experiment for the Cluster mission, *Sp. Sci. Rev.*, *79*, 137–156.

Horne, R. B., G. V. Wheeler, and H. S. C. K. Alleyne (2000), Proton and electron heating by radially propagating fast magnetosonic waves, *J. Geophys. Res.*, *105*, 27,597–27,610, doi:10.1029/2000JA000018.

Horne, R. B., R. M. Thorne, S. A. Glauert, N. P. Meredith, D. Pokhotelov, and O. Santolík (2007), Electron acceleration in the Van Allen radiation belts by fast magnetosonic waves, *Geophys. Res. Lett.*, *34*, L17,107, doi:10.1029/2007GL030267.

Karpman, V. I., and D. R. Shklyar (1972), Nonlinear damping of potential monochromatic waves in an inhomogeneous plasma, *Sov. Phys. JETP*, *35*(3), 500–505.

Karpman, V. I., Y. N. Istomin, and D. R. Shklyar (1974), Nonlinear theory of a quasi-monochromatic whistler mode packet in inhomogeneous plasma, *Plasma Physics*, *16*(8), 685–703, doi:10.1088/0032-1028/16/8/001.

Laakso, H., H. Junginger, R. Schmidt, A. Roux, and C. de Villedary (1990), Magnetosonic waves above  $f_c(H^+)$  at geostationary orbit - GEOS 2 results, *J. Geophys. Res.*, *95*, 10,609–10,621, doi:10.1029/JA095iA07p10609.

Li, W., R. M. Thorne, J. Bortnik, Y. Y. Shprits, Y. Nishimura, V. Angelopoulos, C. Chaston, O. Le Contel, and J. W. Bonnell (2011), Typical properties of rising and falling tone chorus waves, *Geophys. Res. Lett.*, *38*, L14,103, doi:10.1029/2011GL047925.

Ma, Q., W. Li, L. Chen, R. M. Thorne, C. A. Kletzing, W. S. Kurth, G. B. Hospodarsky, G. D. Reeves, M. G. Henderson, and H. E. Spence (2014), The trapping of equatorial magnetosonic waves in the earth's outer plasmasphere, *Geophys. Res. Lett.*, *41*, 6307–6313, doi:10.1002/2014GL061414.

Meredith, N. P., R. B. Horne, and R. R. Anderson (2008), Survey of magnetosonic waves and proton ring distributions in the earth's inner magnetosphere, *J. Geophys. Res. (Space Physics)*, *113*(A6), A06213, doi:10.1029/2007JA012975.

Min, K., and K. Liu (2016), Understanding the growth rate patterns of ion Bernstein instabilities driven by ring-like proton velocity distributions, *J. Geophys. Res. (Space Physics)*, doi:10.1002/2016JA022524, 2016JA022524.

Mourenas, D., A. V. Artemyev, O. V. Agapitov, and V. Krasnoselskikh (2013), Analytical estimates of electron quasi-linear diffusion by fast magnetosonic waves, *J. Geophys. Res. (Space Physics)*, *118*, 3096–3112, doi:10.1002/jgra.50349.

Nakamura, S., Y. Omura, S. Machida, M. Shoji, M. andNose, and V. Angelopoulos (2014), Electromagnetic ion cyclotron rising tone emissions observed by THEMIS probes outside the plasmopause, *J. Geophys. Res. (Space Physics)*, *119*(3), 1874–1886, doi:10.1002/2013JA019146.

Němec, F., O. Santolík, K. Gereová, E. Macúšová, Y. de Conchy, and N. Cornilleau-Wehrin (2005), Initial results of a survey of equatorial noise emissions observed by the Cluster spacecraft, *Planet. Sp. Sci.*, *53*, 291–298, doi:10.1016/j.pss.2004.09.055.

Němec, F., O. Santolík, Z. Hrbáčková, J. S. Pickett, and N. Cornilleau-Wehrin (2015), Equatorial noise emissions with quasiperiodic modulation of wave intensity, *J. Geophys. Res. (Space Physics)*, *120*, 2649–2661, doi:10.1002/2014JA020816.

O'Brien, T. P., and M. B. Moldwin (2003), Empirical plasmopause models from magnetic indices, *Geophys. Res. Lett.*, *30*(4), 1152, doi:10.1029/2002GL016007.

Olsen, R. C., S. D. Shawhan, D. L. Gallagher, C. R. Chappell, and J. L. Green (1987), Plasma observations at the earth's magnetic equator, *J. Geophys. Res.*, *92*, 2385–2407, doi:10.1029/JA092iA03p02385.

Omura, Y., Y. Katoh, and D. Summers (2008), Theory and simulation of the generation of whistler-mode chorus, *J. Geophys. Res. (Space Physics)*, *113*, A04223, doi:10.1029/2007JA012622.

Pedersen, A., P. Décréau, C.-P. Escoubet, G. Gustafsson, H. Laakso, P.-A. Lindqvist, B. Lybekk, A. Masson, F. Mozer, and A. Vaivads (2001), Four-point high time resolution information on electron densities by the electric field experiments (efw) on Cluster, *Annales Geophysicae*, *19*, 1483.

Perraut, S., A. Roux, P. Robert, R. Gendrin, J. A. Sauvaud, J. M. Bosqued, G. Kremser, and A. Korth (1982), A systematic study of ulf waves above  $f_{H^+}$  from geos 1 and 2 measurements and their relationship with proton ring distributions, *J. Geophys. Res. A*, *87*, 6219.

Roberts, C. S., and M. Schulz (1968), Bounce resonant scattering of particles trapped in the Earth's magnetic field, *J. Geophys. Res.*, *73*(23), 7361–7376.

Russell, C. T., R. E. Holzer, and E. J. Smith (1969), OGO 3 observations of ELF noise in the magnetosphere: 1. spatial extent and frequency of occurrence, *J. Geophys. Res.*, *74*, 755, doi:10.1029/JA074i003p00755.

Russell, C. T., R. E. Holzer, and E. J. Smith (1970), OGO 3 observations of ELF noise in the magnetosphere: 2. the nature of the equatorial noise, *J. Geophys. Res.*, *75*, 755, doi:10.1029/JA075i004p00755.

Santolík, O., J. S. Pickett, D. A. Gurnett, M. Maksimovic, and N. Cornilleau-Wehrin (2002), Spatiotemporal variability and propagation of equatorial noise observed by Cluster, *J. Geophys. Res. A*, *107*(A12), 43–1, doi:10.1029/2001JA009159.

Shklyar, D., and H. Matsumoto (2009), Oblique whistler-mode waves in the inhomogeneous magnetospheric plasma: Resonant interactions with energetic charged particles, *Surv. Geophys.*, *30*(2), 55–104, doi:10.1007/s10712-009-9061-7.

Trakhtengerts, V. V., A. G. Demekhov, E. E. Titova, B. V. Kozelov, O. Santolik, E. Marcusova, D. A. Gurnett, J. S. Pickett, M. J. Ryecroft, and D. Nunn (2007), Formation of vlf chorus frequency spectrum: Cluster data and comparison with the backward wave oscillator model, *Geophys. Res. Lett.*, *34*, L02,104, doi:10.1029/2006GL027953.

Trakhtengerts, V. Y. (1995), Magnetosphere cyclotron maser: Backward wave oscillator generation regime, *J. Geophys. Res.*, *100*(9), 17,205–17,210.

Trakhtengerts, V. Y. (1999), A generation mechanism for chorus emission, *Annales Geophysicae*, *17*, 95–100.

Trakhtengerts, V. Y., A. G. Demekhov, E. E. Titova, B. V. Kozelov, O. Santolik, D. Gurnett, and M. Parrot (2004), Interpretation of cluster data on chorus emissions using the backward wave oscillator model, *Physics of Plasmas*, *11*(4), 1345–1351, doi:10.1063/1.1667495.

Tsurutani, B. T., B. J. Falkowski, J. S. Pickett, O. P. Verkhoglyadova, O. Santolik, and G. S. Lakhina (2014), Extremely intense ELF magnetosonic waves: A survey of polar observations, *J. Geophys. Res. (Space Physics)*, *119*, 964–977, doi:10.1002/2013JA019284.

Walker, S. N., and I. Moiseenko (2013), Determination of wave vectors using the phase differencing method, *Annales Geophysicae*, *31*(9), 1611–1617, doi:10.5194/angeo-31-1611-2013.

Walker, S. N., M. A. Balikhin, D. R. Shklyar, K. H. Yearby, P. Canu, C. M. Carr, and I. Dandouras (2015a), Experimental determination of the dispersion relation of magnetosonic waves, *J. Geophys. Res. (Space Physics)*, *120*(11), 9632–9650, doi:10.1002/2015JA021746.

Walker, S. N., M. A. Balikhin, P. Canu, N. Cornilleau-Wehrin, and I. Moiseenko (2015b), Investigation of the chirikov resonance overlap criteria for equatorial magnetosonic waves, *J. Geophys. Res. (Space Physics)*, *120*, 8774–8781, doi:10.1002/2015JA021718.

Woolliscroft, L. J. C., H. S. C. Alleyne, C. M. Dunford, A. Sumner, J. A. Thompson, S. N. Walker, K. H. Yearby, A. Buckley, S. Chapman, and M. P. Gough (1997), The Digital Wave Processing Experiment on Cluster, *Sp. Sci. Rev.*, *79*, 209–231, doi:10.1023/A:1004914211866.

Zhima, Z., L. Chen, H. Fu, J. Cao, R. B. Horne, and G. Reeves (2015), Observations of discrete magnetosonic waves off the magnetic equator, *Geophys. Res. Lett.*, *42*(22),

Accepted Article



**Table 1.** Locations of the Cluster satellites during the events discussed.

Date	Time (UT)	Satellite	MLT (hours)	MLat (degrees)	Distance (Re)
2005-08-18	13:50->14:00	1	13.42->13.46	-8.0->-3.4	5.01->4.93
	13:00-13:30	2	13.03->13.21	-7.4-> 8.5	4.87->4.69
2005-09-16	03:35-04:00	1	11.89->11.82	-5.7-> 4.2	4.72->4.64
	02:50-03:00	2	11.55->11.52	-3.2-> 4.2	4.62->4.58
2005-09-13	17:55-18:05	1	12.18->12.13	-4.7-> 1.6	5.03->4.89
2006-09-17	14:15-14:45	3	11.77->11.83	-18.4->4.46	4.67->4.08

**Table 2.** Frequency spacings of the sporadic harmonic emissions observed on September 17, 200617 September 2006 by Cluster 1.

Start times (UT)	Stop times (UT)	$\delta f$ (Hz)	$\Omega_P$ (Hz)	L-shell (Re)	$\lambda$ (deg)
14:12:09	14:12:47	4.2	4.7	4.1	-1.2
14:15:09	14:15:29	4.3	4.8	4.1	0.6
14:20:19	14:21:18	4.5	5.0	4.0	4.3
14:22:03	14:22:44	4.8	5.1	4.0	5.4
14:23:32	14:23:54	5.5	5.1	4.0	10.5
14:35:14	14:35:47	5.7	5.6	4.2	14.6
14:36:22	14:36:43	5.9	5.6	4.2	15.4
14:38:46	14:39:04	6.5	5.7	4.2	17.1
14:39:37	14:40:00	6.6	5.8	4.3	17.8

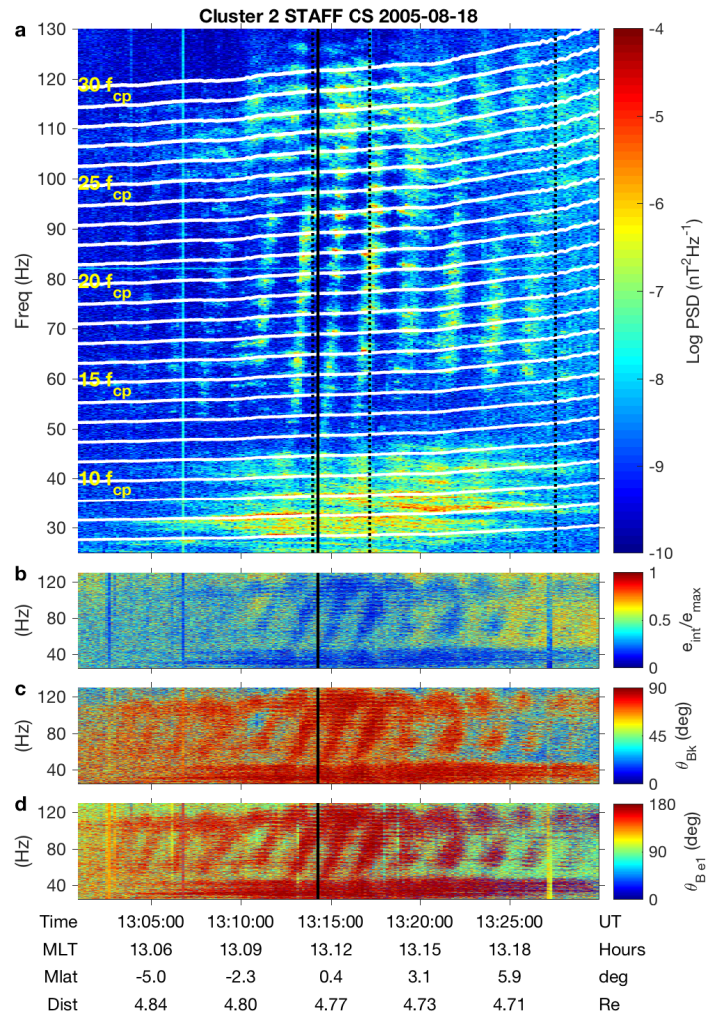


**Figure 1.** Wave properties of the oscillations recorded in the  $B_z$  component by the STAFF search coil magnetometer during the period 13:00-13:30 UT on 18 August 2005. Panel (a) shows a spectrogram of the magnetic measurements. The white lines represent harmonics of the local proton gyrofrequency in the range 7 to 30. Panel (b) shows the ellipticity of the oscillations, panel (c) the angle between the wave propagation vector and the external magnetic field, and panel (d) the angle between the maximum variance direction and the external magnetic field. The vertical black line indicates the equatorial crossing time.

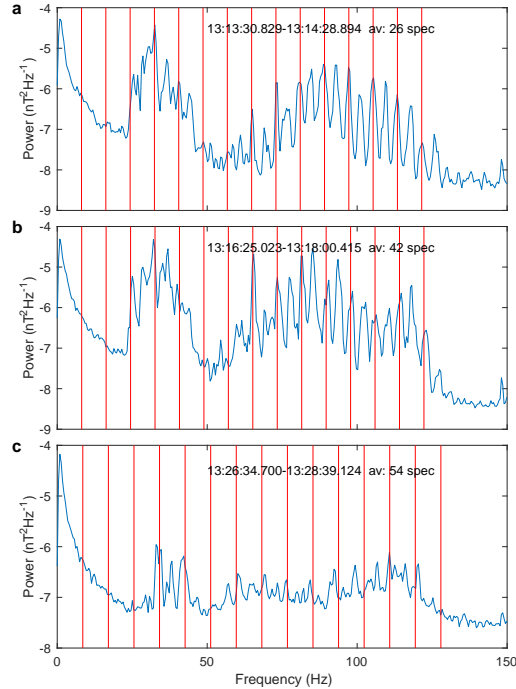


**Figure 2.** Frequency structure of the oscillations in the  $B_z$  component by the STAFF search coil magnetometer during the period 13:00-13:30 UT on 18 August 2005. The vertical red lines indicate every second harmonic of the local proton gyrofrequency in the range 2-30. The power spectral density was calculated using a 1024 point Fast Fourier Transform. Panel (a) shows an average of 26 spectra resulting from the analysis of the waveform, recorded between 13:13:30.8 and 13:14:28.9 UT with a 1024 point fast Fourier Transform. Panels (b) and (c) show similar results for the periods 13:16:25.0-13:18:00.4 UT (average of 42 spectra) and 13:26:34.7-13:28:39.1 UT (54 spectra), respectively.

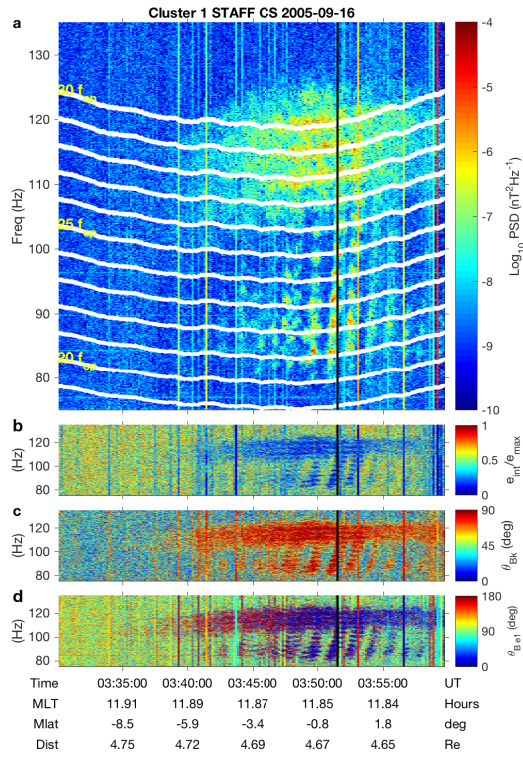


**Figure 3.** Wave properties of the oscillations recorded in the  $B_z$  component by the STAFF search coil magnetometer during the period 03:30-04:00 UT on 16 September 2005. The format is the same as that in Figure 1.

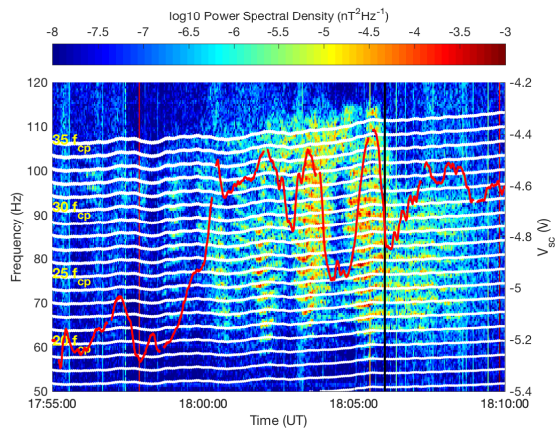


**Figure 4.** A comparison of the wave spectrogram with measurements of the spacecraft potential by Cluster 1 for the period 17:55 to 18:10 UT on 13 September 2005. The red line denotes the spacecraft potential, while the horizontal white lines indicate harmonics of the proton gyrofrequency.

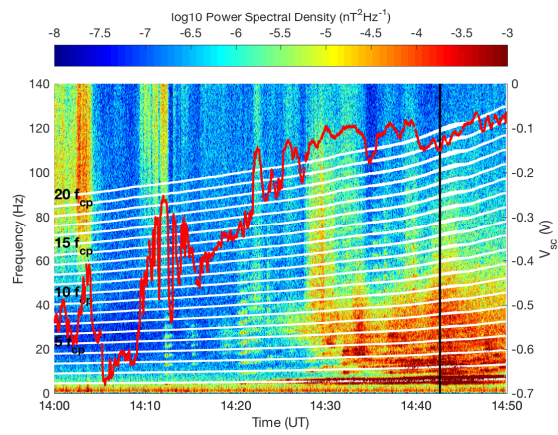


**Figure 5.** A comparison of the wave spectrogram with measurements of the spacecraft potential by Cluster 3 for the period 14:00 to 15:00 UT on 17 September 2006. The format is the same as used in Figure 4.

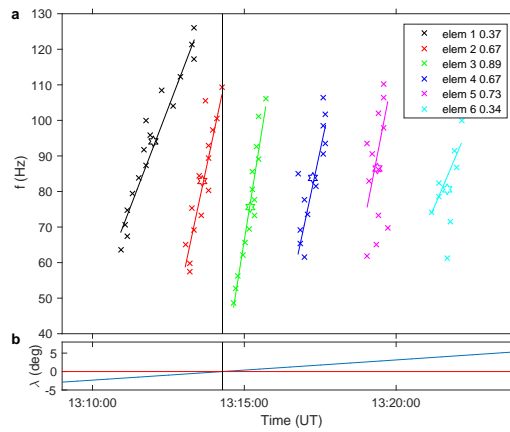


**Figure 6.** A comparison of the frequency sweep rates of the rising tone elements observed by Cluster 2 on 18 August 2005. Panel (a) shows the frequency sweep rate of the individual elements observed in the vicinity of the geomagnetic equator. The gradients of the individual elements are shown in the legend. Panel (b) shows the magnetic latitude of Cluster 2 for comparison.



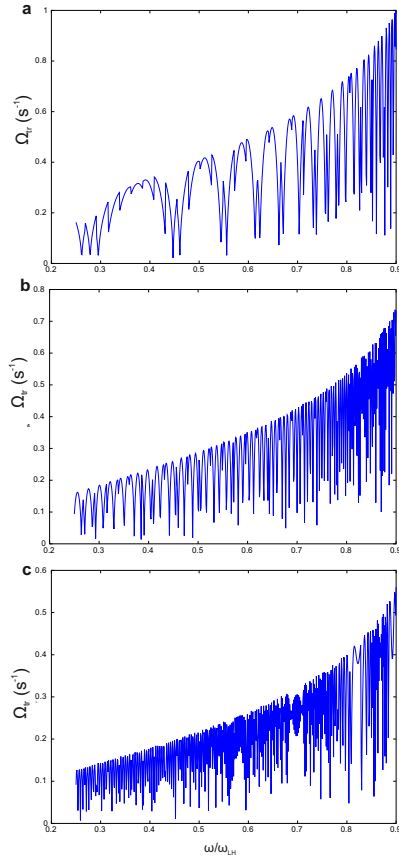


**Figure 7.** The trapping frequency  $\Omega_{tr}$  for suprathermal protons in the field of MS waves: upper, middle, and lower panels show the result for proton perpendicular energies of 0.1, 1, and 10 keV, respectively.

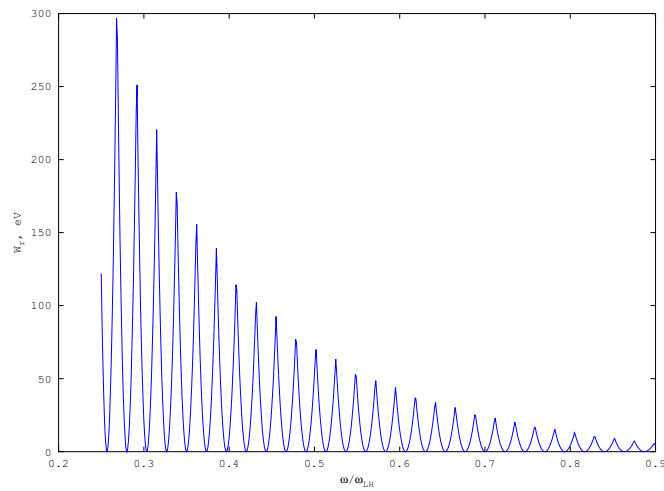


**Figure 8.** Resonant parallel energy of protons depending on the MS wave frequency for the same conditions as in Fig. 7. The resonance number for the given frequency is chosen according to the gyroharmonic closest to this frequency.